



RESEARCH ARTICLE

10.1002/2015WR018292

Key Points:

- Fully automated LSPIV processing chain relying on photogrammetric measurements only
- Redundant measurements and statistical calibration reduce mean absolute percentage error to 9%
- Long-term study with >4000 videos and measurements of discharge dynamics during tropical cyclones

Supporting Information:

- Supporting Information S1
- Figure S1
- Figure S2

Correspondence to:

A. Stumpf,  
andre.stumpf@unistra.fr

Citation:

Stumpf, A., E. Augereau, C. Delacourt, and J. Bonnier (2016), Photogrammetric discharge monitoring of small tropical mountain rivers: A case study at Rivière des Pluies, Réunion Island, *Water Resour. Res.*, 52, 4550–4570, doi:10.1002/2015WR018292.

Received 26 OCT 2015

Accepted 10 MAY 2016

Accepted article online 13 MAY 2016

Published online 18 JUN 2016

# Photogrammetric discharge monitoring of small tropical mountain rivers: A case study at Rivière des Pluies, Réunion Island

André Stumpf<sup>1,2,3</sup>, Emmanuel Augereau<sup>1</sup>, Christophe Delacourt<sup>1</sup>, and Julien Bonnier<sup>4</sup>

<sup>1</sup>Laboratoire Domaines Océaniques, CNRS UMR 6538, Institut Universitaire Européen de la Mer, Plouzané, France,

<sup>2</sup>Laboratoire Image, Ville, Environnement, CNRS UMR 7362, University of Strasbourg, Strasbourg, France, <sup>3</sup>Institut de

Physique du Globe de Strasbourg, CNRS UMR 7516, University of Strasbourg, Strasbourg, France, <sup>4</sup>Office de l'eau Réunion, Service Ressource en eau, Saint-Denis, France

**Abstract** Reliable discharge measurements are indispensable for an effective management of natural water resources and floods. Limitations of classical current meter profiling and stage-discharge ratings have stimulated the development of more accurate and efficient gauging techniques such as nonintrusive photogrammetric techniques. Despite many successful applications of large-scale particle image velocimetry (LSPIV) for short-term measurements during flood events, there are still very few studies that address its use for long-term monitoring of small mountain rivers. To fill this gap, this study targets the development and testing of largely autonomous photogrammetric discharge measurement system with a special focus on the application to small mountain river with high discharge variability in the tropics. It proposes several enhancements concerning camera calibration, more efficient processing in image geometry, the automatic detection of the water level as well as the statistical calibration and estimation of the discharge from multiple profiles. A case study which comprises the analysis of several thousand videos spanning over 2.5 year is carried out to test the robustness and accuracy of different processing steps. Comparisons against classical current meter profiling show a mean absolute percentage error of 9.0% after the statistical calibration of the system. The study suggests that LSPIV can already be considered as a valuable tool for the monitoring of torrential flows, whereas further research is still needed to fully integrate nighttime observation and stereo-photogrammetric capabilities.

## 1. Introduction

Monitoring river discharge is a crucial task for the management of water resources, the assessment of natural hazard, and hydrological as well as geomorphological studies. While most major rivers in developed countries are being gauged with classical velocity-area or rating-curve methods the total number of discharge gauging and sediment sampling stations has decreased considerably in recent decades readily affecting the quantification and prediction of river discharge [Milliman and Farnsworth, 2011]. Especially for small mountain river catchments in the tropics, the data situation is still very sparse while, at the same time, such catchments have a disproportional large contribution to the sediment transfer [Milliman, 1995]. Existing records, in addition, bear high uncertainties between 5% and 40% depending on study site [Baldassarre and Montanari, 2009; Hamilton and Moore, 2012; McMillan et al., 2012]. Especially at sites with dominantly torrential runoff, it remains challenging to establish reliable rating-curves due to very few available records for events with high magnitude and low frequency.

To address such issues, considerable efforts have already been made to develop versatile measurement systems based on radar and acoustic waves. In particular, acoustic Doppler current profilers (ADCPs) are now widely used for operational discharge measurements and scientific research [Parsons et al., 2013]. Mobile ADCPs, however, target mainly repeated surveys along major rivers and are not entirely suitable to permanently monitor creeks and small mountain rivers with torrential character. Surface velocity radar (SVR) has shown promising results for gauging also smaller mountain creeks but is less suitable for measurements during rainfall and provides only limited spatial resolution [Welber et al., 2016].

An alternative nonintrusive method is LSPIV [Fujita *et al.*, 1998], which is based on image correlation to determine the surface flow velocity from video sequences. LSPIV has already been tested in numerous studies including initial proof-of-concept implementations [Creutin *et al.*, 2003; Bradley *et al.*, 2002], the assessment of measurement uncertainties through detailed field case studies [Kim, 2006; Le Coz *et al.*, 2010; Dramais *et al.*, 2011], numerical simulations [Hauet *et al.*, 2008a], and laboratory tests on shallow flow conditions [Legout *et al.*, 2012]. Muste *et al.* [2008] provided a comprehensive review of the development and applications of LSPIV and stated error rates ranging from 2% to 35%. While different sources of measurement uncertainties are well understood there are still very few studies targeting real-time discharge monitoring [Hauet *et al.*, 2008b; Le Coz *et al.*, 2010] or the use of standard surveillance cameras to gauge major floods during rainstorms [Tsubaki *et al.*, 2011]. As the first LSPIV systems become commercially available, it becomes increasingly important to better understand their potential and limitations for operational use.

Indeed, many previous works have focused mainly on the use of LSPIV systems for relatively short-term observations [Kim *et al.*, 2008; Le Coz *et al.*, 2010; Dramais *et al.*, 2011; Jodeau *et al.*, 2008; Fujita *et al.*, 2007; Muste *et al.*, 2011] and did therefore not fully address some major challenges for operational photogrammetric discharge monitoring. This comprises for example variable illumination and flow conditions which are generally challenging for any automated image processing chain. Especially in gravel bed rivers, further issues can arise from the high mobility of the riverbed which will affect the volume calculations. As already noted by Hauet *et al.* [2008b], LSPIV techniques also depend on measurements of the water surface height from additional pressure gauges or nearby gauging stations which adds constraints on the site selection and additional requirements for field installations. Finally, challenges also concern technical aspects such as the robustness of the system when exposed to temperature fluctuations or storms, and the processing and storage of larger volumes of video data when multiple cameras are operated at short intervals.

To progress further toward an operational use of photogrammetric discharge measurements, the presented study addresses several of the outlined issues with a strong focus on the monitoring of small torrential mountain rivers in tropical environments. It comprises some innovative aspects regarding the design of the acquisition system and reconstruction of the riverbed topography, whereas the main focus of this study is the development and testing of a processing chain that allows robust, accurate, and efficient photogrammetric discharge measurements. This comprises several enhancements among previously proposed LSPIV techniques including lens calibration with radial distortion parameters, image processing in the image geometry which eliminates the need to rectify each single video frame, the estimation of the water surface level directly from the video stream and the riverbed topography, and the robust estimation of the discharge through spatial averaging of multiple profiles.

The remainder of this article first introduces the particular challenges at the study site (section 2) and explains the system setup and the data collection (sections 2.1–2.2). Section 3 details all steps in the photogrammetric processing chains including the camera calibration, the riverbed reconstruction, the estimation of the water level, and the computation of the discharge. It also explains the protocols for the assessment of uncertainties and errors in the results. The obtained results as well as the potential and limitations of the proposed system are discussed in section 4 and conclusions are drawn in section 5.

## 2. Study Site, Instrumentation, and Data

The study site (Figure 1) is a cross section of the Rivière des Pluies on the La Réunion Island located at 20.095°S and 50.506°E. The island features a humid tropical climate and a young volcanic relief with intense geomorphological processes such as lava flows, landslides, flash floods, large debris flows [Garcin *et al.*, 2005], and exceptionally high sediment transfer rates. During the main rainy-season months of January through March, La Réunion is every year impacted by intense tropical cyclones which yield some of the highest rainfall rates in the world [Villeneuve *et al.*, 2014] and frequently have severe impacts on the islands' infrastructure and inhabitants. The personnel of the regional water management department (Office de l'eau Réunion) is typically not allowed to carry out field surveys during such cyclones, which makes it difficult to obtain reliable data on the dynamics of major floods occurring during those periods.

The catchment of the Rivière des Pluies extends over 46 km<sup>2</sup> from 2270 m to sea level and receives an average annual rainfall of 3400 mm [Pouget and Garcin, 2003]. The river is 18.5 km long and the study site is located at kilometer 16 with an upstream catchment of 38.1 km<sup>2</sup>. The mobile gravel riverbed is braided and

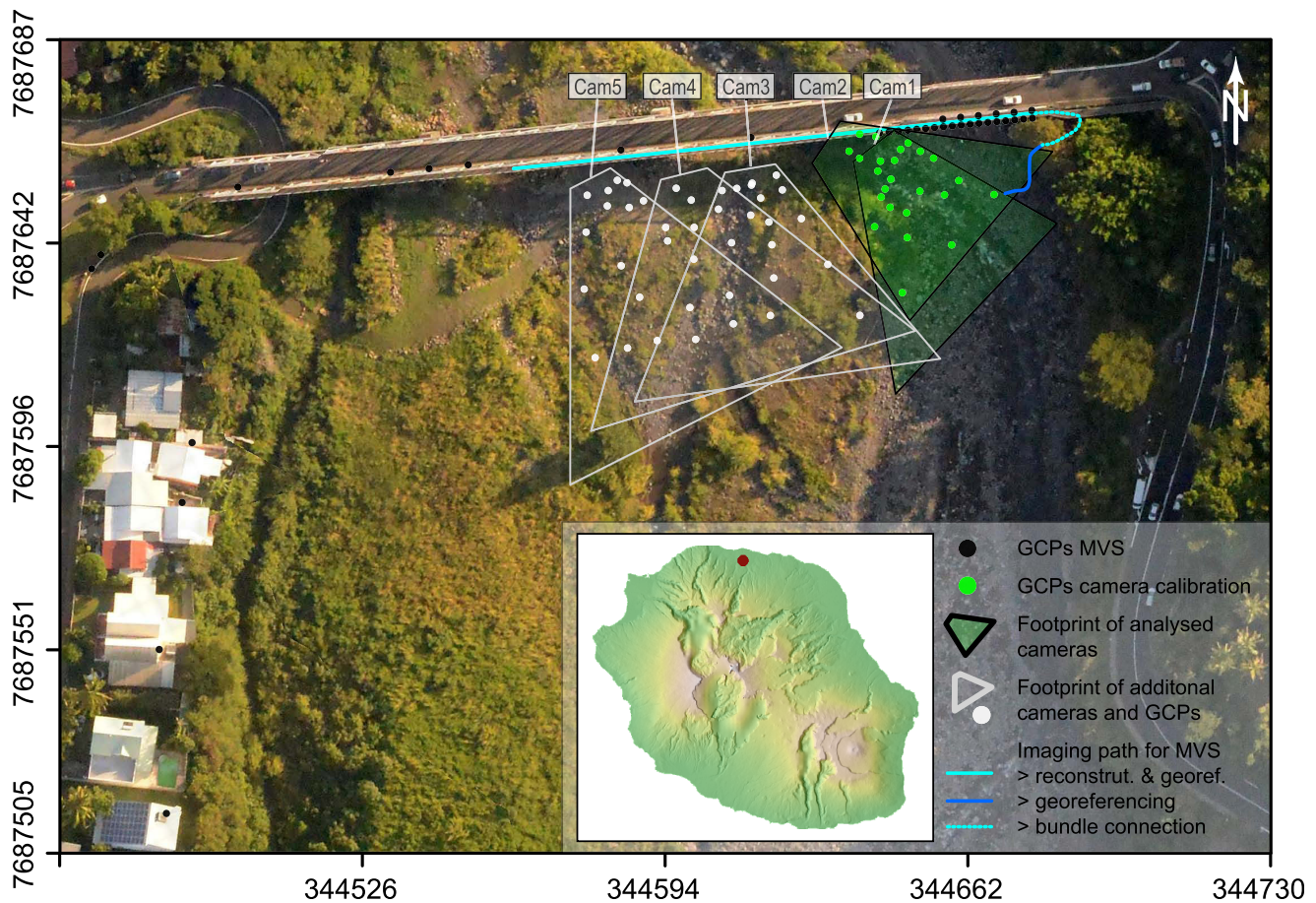


**Figure 1.** Location and overview of the study site at Rivière des Pluies, dGNSS point measurements and footprints of the video recordings.

most of the time only the most eastern branch at the cross section is active (Figure 1). This branch has an average slope of 2.7% and the width of the flow varies between approximately 2 and 45 m from low discharge to flood events. The discharge does typically not exceed a few  $\text{m}^3 \text{s}^{-1}$  throughout most of the year, whereas it has been suggested that the peak discharge can exceed  $1000 \text{ m}^3 \text{ s}^{-1}$  [Pouget and Garcin, 2003] during large flash floods. The combination of environmental factors comprising a tropical climate, a mobile and complex riverbed and a large discharge variability make Rivière des Pluies a challenging study site for the development and application of photogrammetric discharge measurements.

### 2.1. Imaging Systems and Data

The video imaging systems that we installed at the Rivière des Pluies comprise a total of five video surveillance cameras including three Axis P1344-E with a fixed view angle (Cam1, Cam3, Cam5) and two Axis Q6032-E with pan-tilt-zoom capabilities (Cam2, Cam4). The image resolution of those two models is  $640 \times 480$  pixel and  $720 \times 576$  pixels, respectively. The videos are recorded with an average frame rate of 25 fps. The electric power supply for the on-site system comprises four 12 V batteries which are being recharged by a 200 W solar panel during the day and are also connected to the local street light power grid for additional charging during nighttime. Recorded videos are transferred in real time via a directional Wifi antenna to a facility of the University of Reunion Island 1 km to west where all videos are stored and processed directly on a local server. The server and the Wifi are connected to an uninterruptible power supply (UPS). Consequently, the system can operate autonomously for approximately 3 days which is critical for continuous acquisitions during failures of the central power grid frequently occurring during passages of tropical cyclones. The processing results are downloaded through a VPN connection which also allows remote modifications of the acquisition protocols and maintenance.

**Table 1.** Overview of the Topographic Data Sources Being Multiview Stereophotogrammetry (MVS), Terrestrial Laser Scans (TLS), and Differential Global Navigations Satellite System (dGNSS)

Date	MVS	TLS	dGNSS
5 Nov 2013	Nikon D800, 184 images, 7878 × 4924 pixels	Riegl VZ-400, ~7 million points	30 points on stable terrain recorded on 2 Dec 2014
13 May 2014			Topcon HiperII, 15 points in the riverbed, RMSE = 3.9 cm
2 Dec 2014	Nikon D800, 388 images, 7878 × 4924 pixels	Riegl VZ-400, ~7 million points	Topcon HiperII, 25 points in the riverbed, 30 points on stable terrain, RMSE = 3.9 cm
28 May 2015			Topcon HiperII, 15 points in the riverbed, RMSE = 3.9 cm

The cameras are oriented at fixed angles in the upstream direction with partially overlapping footprints to enable redundant measurements (Figure 1). The analyses presented in this paper will focus mainly on Cam1 and Cam2 since during the monitoring period discharge concentrated in the view field of these cameras. Only at one occasion flow was also observed at one of the other cameras and integrated in the final discharge estimate. Regular video acquisitions have started in December 2012. Videos were initially recorded approximately every 2 weeks and the frequency was only increased during high discharge events. This operation was maintained during 2013 and 2014 to test the long-term stability of the system and obtain video material for the development of the processing chain. Since late 2014, the recording frequency has been increased to half hour intervals. This is regarded as the best possible balance between a high temporal resolution, the available power supply, the network bandwidth, and the processing time. A total number of 4218 videos with an average length of 15 s each, have been analyzed for this study.

The developed processing chain depends on topographic models covering the imaged riverbed, which were obtained using both multiview stereophotogrammetry (MVS) and terrestrial laser scans (TLS). An overview of the acquired data sets is given in Table 1. For the MVS reconstruction of the riverbed, photographs have been recorded on two dates (5 November 2013 and 2 December 2014) with views from the bridge southward down into the riverbed, views from the riverbed northward to the bridge as the main stable reference, and a couple of views connecting between the two linear configurations (Figure 1). The photographs were acquired with a Nikon D800 equipped with a 35 mm lens and the focus set to infinity.

### 2.2. Terrestrial Laser Scans (TLSs) and dGNSS Surveys

Terrestrial laser scans of the riverbed were carried out on 13 May 2013 and 28 May 2015 with a Riegl VZ-400 positioned on the bridge 10 m above the riverbed. During the scans, the flow depth was less than 10 cm and the water was calm and clear. Meeting these conditions allowed a reasonable number of ground points in submerged areas and resulted in a low incidence angle to reduce possible refraction effects [Heritage and Hetherington, 2007]. The device features a rotating head scan mode which allows scanning the entire surface in the area of interest with one scan. The scan frequency was set to 120 kHz which corresponds to a precision of 5 mm at a scanning distance of 100 m and a maximum range of 400 m. The resulting point cloud contains 7 million points. The resulting point clouds were georeferenced using RiSCAN PRO and 15 ground control points (GCPs), marked by artificial reflector targets, were evenly distributed in the riverbed. Nonground points (mainly vegetation) were removed manually.

The GCPs were collected with a Topcon HiperII dGNSS system in real-time kinematic mode. The acquisition frequency was set to 1 Hz and each target was measured during at least 20 s. Postprocessing was performed using the GrafNet software and a fixed base station located at a distance of 17 km and 100 m above the surveyed site. The global root-mean-squared error (RMSE) of the computed ground coordinates was estimated at 3.9 cm.

### 3. Methods

In the classical velocity-area method, discharge is determined through the integration of measured stream velocities over the channel cross section. The processing chain in this study targets to quantify all required variables (stage, velocity, and wetted surface area) based on the automatic analysis of the video stream and the bed topography derived from MVS or TLS. This includes several interrelated processing steps being

camera calibration, the reconstruction of the riverbed, water surface detection, water level estimation, and the calculation and calibration of the discharge. An overview of those processing chain is given in Figure 2 and the individual steps are described in the following subsections. The implementation of the processing chain relies largely on MATLAB [MathWorks, 2014] and the FFmpeg library [ffmpeg.org, 2015].

### 3.1. Camera Calibration

Most previous studies have used a direct linear model for the mapping between image and ground coordinates [e.g., Fujita et al., 1998; Muste et al., 2008]. While the use of a linear relationship is straightforward, it does not allow to compensate radial lens distortion, which leads to important projection errors if the camera features a wide view angle and a nonnegligible radial distortion [Le Boursicaud et al., 2016; Remondino and Fraser, 2006].

To address this issue, we adopt the two-step calibration technique proposed by Tsai [1987] which—in addition to the exterior orientation  $[\mathbf{R} \mid \mathbf{t}]$ , focal length  $f$ , skew factor  $s$ , and the principal point  $x_0, y_0$ —allows to estimate a parameter for radial lens distortion  $L(\tilde{r})$ . The estimation of all parameters is achieved in two separate steps and requires a minimum of nine reference points with known coordinates in the image plane and 3-D cartographic coordinates. An initial estimate of the camera parameters is obtained using a least square fit and the initial estimates are subsequently refined using an iterative Levenberg-Marquardt solver [Salvi et al., 2002]. The number of available GCPs was 18 for Cam1 and 20 for Cam2. In addition, the technique requires precise information on the number of pixels and their metric size along the row and columns of the imaging device.

The obtained parameters establish a relationship between the pixel coordinates in the image plane and the 3-D cartographic coordinates  $(X_w, Y_w, Z_w)$  which in a simplified form can be denoted as in equation (1).

$$\begin{bmatrix} x_h \\ y_h \\ z_h \end{bmatrix} = \begin{bmatrix} f & s & x_0 \\ 0 & f & y_0 \\ 0 & 0 & 1 \end{bmatrix} [\mathbf{R} \mid \mathbf{t}] \begin{bmatrix} X_w \\ Y_w \\ Z_w \\ 1 \end{bmatrix} \tag{1}$$

Here  $(x_h, y_h, z_h)$  are the image coordinates expressed as a homogeneous vector. The homogeneous coordinates can be converted to image coordinates  $(\tilde{x}_{im}, \tilde{y}_{im})$  using equation (2).

$$\tilde{x}_{im} = \frac{x_h}{z_h} \quad \text{and} \quad \tilde{y}_{im} = \frac{y_h}{z_h} \tag{2}$$

This transformation corresponds to the classical direct linear transform which does not take into account lens distortion. The relationship between the linearly projected and the real image coordinates (i.e., corrected for radial distortion) is given by equation (3).

$$\begin{pmatrix} x_{im} \\ y_{im} \end{pmatrix} = L(\tilde{r}) \begin{pmatrix} \tilde{x}_{im} \\ \tilde{y}_{im} \end{pmatrix} \tag{3}$$

where  $\tilde{r}$  is the radial distance  $\sqrt{x^2 + y^2}$  from the center of the radial distortion and  $L(\tilde{r})$  is the distortion factor as a function of the radius  $\tilde{r}$  [Hartley and Zisserman, 2004], which is determined during the iterative calibration outlined above.

Most previous studies have used a direct linear transformation to project all video frames into the ground geometry (pseudo-orthorectification) and subsequently used image velocimetry to measure the surface velocities. This, however, requires an additional resampling step which can lead to artefacts in the measured velocities [Inglada et al., 2007] and extreme distortions in the far view field [Dramais et al., 2011]. Such issues can be circumvented considering that the described mapping between ground and image coordinates allows both, to determine the coordinates of a given pixel on the ground, and to project a given ground coordinate into the image geometry. To avoid resampling artefacts and image distortions, the equations are thus used to project the 3-D model of the riverbed into the image geometry (section 3.2), and to determine the physical size of each pixel on the ground (section 3.6).

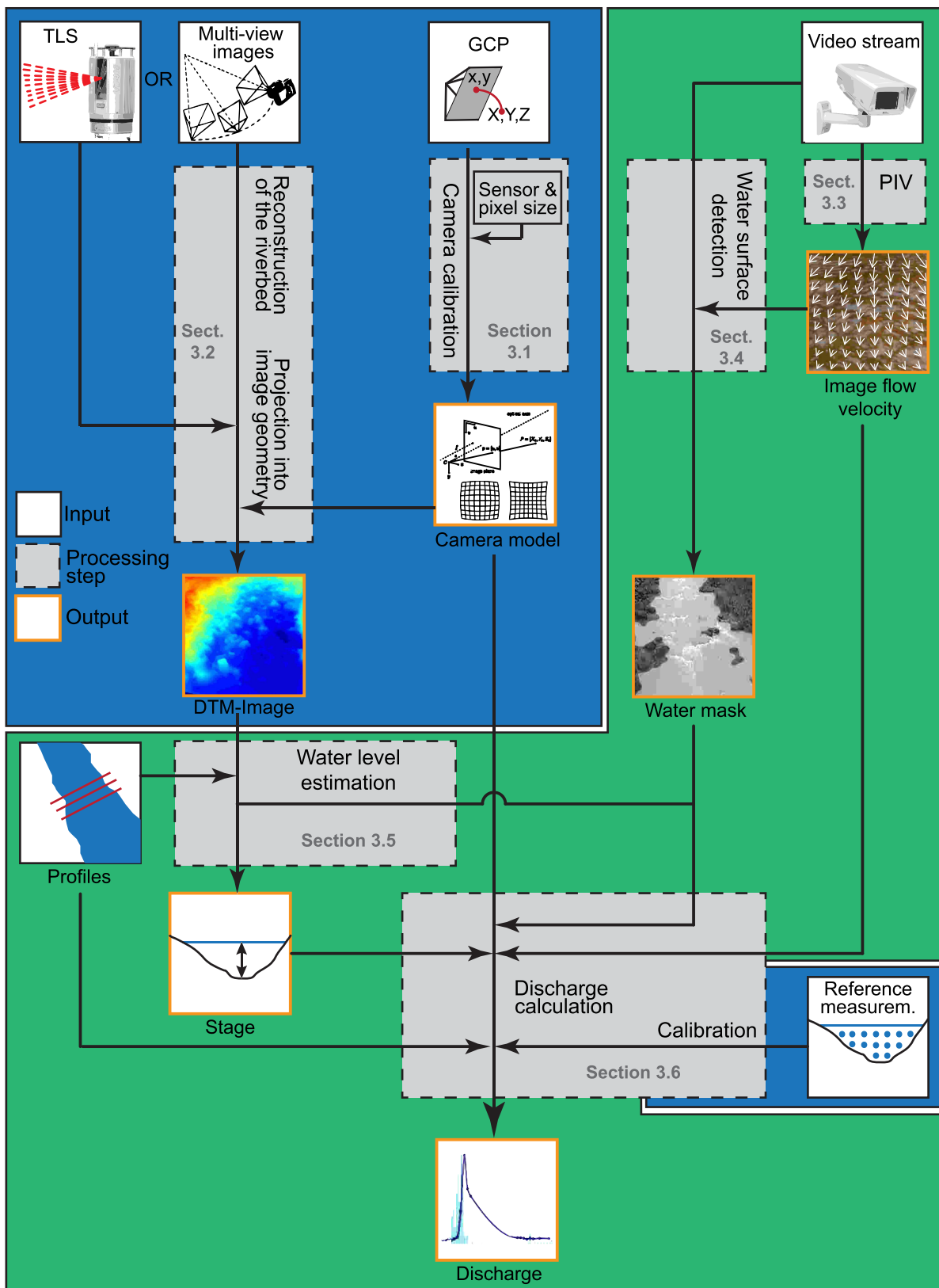


**Figure 2.** Overview of the photogrammetric processing chain showing the interdependencies of all offline (before operation, blue background) and online (during operation, green background) processing steps. The sections which detail the respective processing steps are indicated within the grey boxes. TLS = terrestrial laser scan, GCP = ground control points, PIV = particle image velocimetry, and DTM-Image = digital terrain model projected into the image geometry.

### 3.2. Photogrammetric Reconstruction of the Riverbed

The high mobility of the riverbed imposes a need for frequent updates of the topography to ensure accurate estimates of the flow depth and MVS is used as the primary technique for the riverbed reconstruction (5 November 2013 and 2 December 2014). The reconstruction is performed using the open-source library MICMAC [Pierrot-Deseilligny *et al.*, 2015] which has been demonstrated to yield highly accurate 3-D point clouds [Ouedraogo *et al.*, 2014; Stumpf *et al.*, 2015]. To confine the computational load, tie points are extracted at a reduced image resolution of  $2951 \times 1969$  pixels and for each image only the 50 closest neighboring views are matched. The latter can be achieved by referring to the lexicographical order of the image file names since the acquisition geometry follows a linear path leading to an ordered image collection. The relative orientation of all images is subsequently determined with MICMAC's module for bundle-adjustment [Pierrot-Deseilligny and Clery, 2011]. After marking the position of the GCPs, the same module is used to georeference the bundle in the local coordinate system. The 30 GCPs located on stable ground were marked in all images yielding total of 87 unique points for the survey on 5 November 2013 and 201 unique points for the survey of 2 December 2014. Finally, a series of master images is selected to evenly cover the area filmed by the video cameras. For each master image, the closest 10 neighboring views are selected as slave images. For further details on MICMAC's dense reconstruction algorithm, we refer to Pierrot-Deseilligny *et al.* [2015] or Stumpf *et al.* [2015].

The dense reconstruction yields 3-D point clouds in which each point is also associated with an RGB color value [0,255] and a correlation coefficient  $CC$  [0,1] that provides an indicator for the uncertainty of the point. They are used to automatically remove points with low correlation and high ratio of the green channel  $rG$ . More specifically, the indicator  $rG$  can be exploited to detect vegetation [Stumpf *et al.*, 2013] and is defined as  $rG = G/(R + G + B)$  where  $R$ ,  $G$ , and  $B$  are the intensity values of the red, blue, and green channels, respectively. Corresponding threshold conditions are set so that only points with  $CC > 0.6$  and  $rG < 0.33$  are included in the final point cloud. All remaining points are projected into the image plane of the camera using the established calibration parameters. The elevation values of the projected ground points are subsequently interpolated according to the pixel grid of the image using natural neighbor interpolation [Sibson, 1981].

### 3.3. Particle Image Velocimetry

When a video is passed to the correlator, it is initially probed and timestamps with a precision of 1 ms are extracted for all frames. According to the desired number of frames  $n_{fr}$ , the sequence with the highest average frame rate is selected automatically and the time lags of the selected frames  $\Delta_t$  are stored ( $\overline{\Delta_t} \approx 0.04$  s). This allows to compensate altering frame rates typical for standard surveillance cameras, and to filter out bucking video sequences that might otherwise lead to decorrelation or an underestimation of the flow velocity.

Template-matching with normalized cross correlation (NCC) is used to measure the displacement of surface features among successive frames. Initial matches are refined to subpixel precision using a Gaussian peak fit [Willert and Gharib, 1991]. In contrast to many previous studies [e.g., Muste *et al.*, 2008], however, the reprojection of the video frames into the ground geometry is omitted, and the measurements are performed directly in the original image geometry. This leads to a variable pixel footprint in the near field and far field of the cameras ranging from 0.022 to 0.081 m pixel<sup>-1</sup>, respectively. The size of the search template  $w_t$  should be suitable to capture characteristic flow features and a preliminary analysis is conducted to assess the impact of  $w_t$  on the measured surface velocities at different image depths. It shows that the measured surface velocities remain stable over a wide range of intermediate window sizes of 8–12 pixels (supporting information, Figure S1a). The size is consequently fixed at  $w_t = 10$  pixels for all experiments and the search range  $w_b$  in the base frame is constrained to a distance of 20 pixels from the template center, which corresponds to a maximum velocity of approximately 15 m s<sup>-1</sup>. A further set of preliminary experiments showed a stabilization of the mean measured velocities beyond  $n_{fr} = 30$  (supporting information, Figure S1b) and the parameter is consequently fixed at  $n_{fr} = 40$  for all experiments.

The computational cost of image correlation increases linear with the search range and the number of sampled locations  $n_s$ , corresponding to a complexity of  $O(w_b \times n_s)$  where  $n_s$  is the product of the image rows and columns (e.g., 307,200 for Cam1). To alleviate the computational load, matching is performed only

for every tenth row and column of the base image which reduces  $n_s$  by a factor of 100. The average image flow velocity  $\bar{v}_{l_{xy}}$  expressed in pixel  $s^{-1}$  is computed for each measured pixel as in (4).

$$\bar{v}_{l_{xy}} = \frac{1}{n_m} \sum_{i=1}^{n_m} \frac{|\Delta_{xy_i}|}{\Delta t_i} \tag{4}$$

Here  $n_m$  is the number of frames for which  $NCC > 0.6$  ( $n_m \leq n_{fr}$ ) and  $|\Delta_{xy_i}|$  is the Euclidean norm of the displacement vector measured among two successive frames  $i - 1$  and  $i$ . The selected  $NCC$  threshold is rather conservative to retain measurements for most of the sampled grid points.  $NCC$  values of 1, which can sometimes indicate stationary flow features, are only observed occasionally on stable terrain which is why no upper  $NCC$  threshold is used. The flow field is subsequently interpolated for the domain of the input video using natural neighbor interpolation. This method allows for a relatively fast computation and a complete velocity field that is subsequently used in the detection of the water surface and the discharge estimation.

### 3.4. Water Surface Detection

The estimation of the water level is a crucial element for the discharge calculations. Many previous LSPIV studies relied on additional pressure gauges [Le Coz et al., 2010; Dramais et al., 2011; Jodeau et al., 2008] or stage measurements at nearby gauging stations [Hauet et al., 2008b; Kim et al., 2008] to derive the area of the wetted surface from the water level and profiles of the riverbed topography. While devices such as pressure gauges can provide very accurate stage measurements, they are prone to being frequently damaged in torrential streams with mobile riverbeds like Rivière des Pluies. Initial tests with a radar level sensor mounted on the bridge neither provided satisfactory results due to the increasing water surface roughness at high discharges, interference from metallic bridge structures and dry areas in the radar footprint at low discharges. To address this issue, we developed an algorithm for the automatic detection of the water surface and the subsequent statistical estimation of the water level directly from the video stream and the riverbed topography. A similar idea was recently brought forward by Ran et al. [2016] but not pursued with the development of an automatic technique.

Based on the video stream, the following index is computed as a proxy for the likelihood of water being present in a particular pixel.

$$p_{w_{xy}} = (\bar{v}_{l_{xy}} + \sigma_{\bar{B}_{xy}} + (1 - H_{\bar{B}_{xy}}) - rG_{xy})/3 \tag{5}$$

In addition to the variables defined above,  $\sigma_{\bar{B}_{xy}}$  denotes the variance of the mean brightness  $\bar{B}_{xy} = (R + G + B)/3$  over all frames and  $H_{\bar{B}_{xy}}$  is the entropy of the local grey value histogram around the respective pixel  $xy$ . The neighborhood for computing  $H_{\bar{B}_{xy}}$  is a circle with a radius of 5 pixels. The underlying assumptions are that the water surface features a detectable motion and an increased variance. Areas of the water surface which display no visible movement, however, feature a very homogeneous surface texture and a high entropy.  $rG_{xy}$  serves as a penalty for green color presumably representing vegetation. All variables are normalized by their range to an interval of [0,1] before entering the right-hand side of equation (5) and  $p_{w_{xy}}$  hence falls into the same interval.

A threshold  $t_i$  on the indicator  $p_{w_{xy}}$  is determined automatically [Otsu, 1975] and used to initialize a binary mask where  $p_{w_{xy}} \geq t_i$ : 1 and  $p_{w_{xy}} < t_i$ : 0. The binary mask is used to initialize an active contour segmentation [Chan and Vese, 2001] with a contraction bias set to 1 and a morphological filter is subsequently applied to remove positive patches smaller than 2000 pixels. The latter presents the minimum expected water area and targets the removal of isolated false positive detections disconnected from the actual stream.

Before the water mask is used for the water level estimation, a final test is used to compare the brightness of the water with the surrounding gravel bed. The objective of this step is to compensate for changes in the illumination conditions and surface brightness during precipitation events. More specifically under such conditions, the wetted gravel bed becomes darker while the stream itself becomes brighter with increasing turbidity. The mean brightness of all pixels within the water mask ( $\bar{B}_W$ ) is compared against the mean brightness of all nonwater pixels ( $\bar{B}_{nW}$ ) using a two-sampled  $t$  test with a null-hypothesis of equal means. If the null-hypothesis is rejected (i.e., the brightness of the detected water is significantly different from surrounding areas) and if  $\bar{B}_W > \bar{B}_{nW}$  the detection routine is repeated using a modified water index as specified in (6).

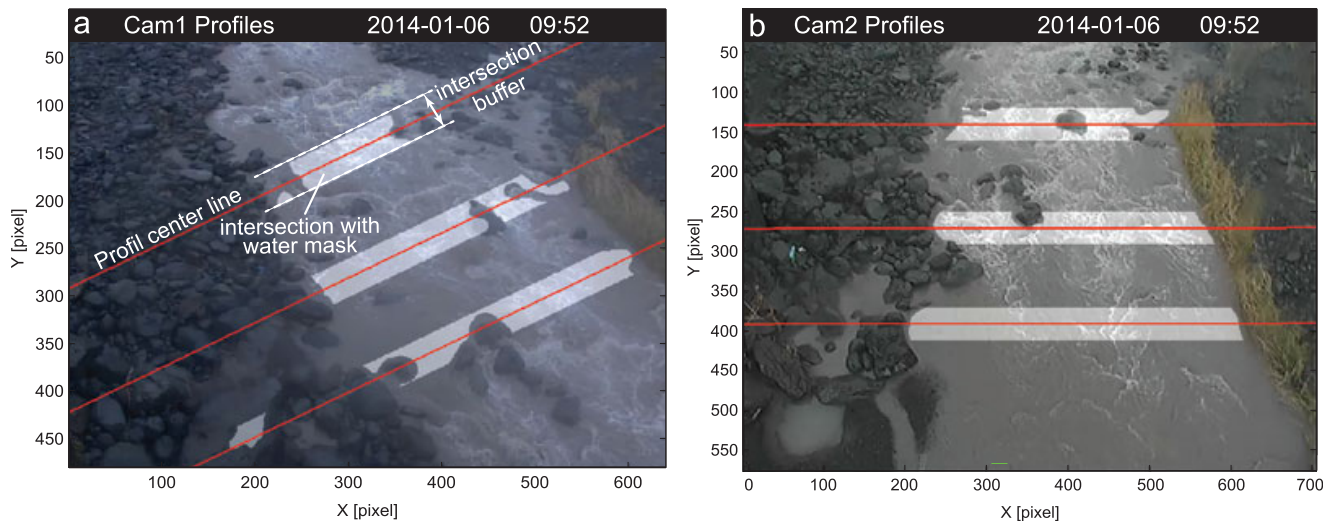


**Figure 3.** Overview of the measurement profiles set for (a) Cam1 and (b) Cam2. The defined center line of each profile is intersected with the water mask to select the pixels which are considered for the estimation of the water level and the discharge.

$$p_{w,xy} = (\bar{v}_{I,xy} + \sigma_{B,xy} + (1 - H_{B,xy}) - rG_{xy} + \bar{B}_{xy}) / 4 \quad (6)$$

We note that the processing chain for the detection of the water surface was developed and parameterized on a subset of 10 videos representative for different discharge conditions. The accuracy and robustness of the proposed algorithm is tested on a total 74 videos for which reference water masks have been created through visual image interpretation by the authors. To this end, an individual frame from each video was loaded into graphics editing software and all pixels belonging to the water surface were marked with a brush tool. The accuracy of the detection is assessed by intersecting the automatically extracted water masks with their manually created references. The number of false positives, false negatives, and true negatives is used to compute precision, recall, and the F1-score which is the harmonic mean of precision and recall [He and Garcia, 2009].

### 3.5. Water Level Estimation

The water height is estimated statistically in image geometry through an overlay of the water mask on the digital terrain model (DTM) projected on the image plane. Figure 3 shows the location of the six fixed profiles in the image geometry and exemplifies the result of an intersection between the defined center lines and the extracted water masks. Thereby a buffer of the size  $d_{xy} = 20$  pixels is used to include all pixels perpendicular to the center line in the buffer. The masks obtained at each profile are intersected with the projected DTM to observe the distribution of the bed elevation values  $Z$  along the profile where the highest values should depict the local water level elevation  $z_w$ . The distribution maximum, however, is generally very susceptible to outliers and likely to yield an overestimation of the water level.

In order to obtain reliable estimates of the water level, robust measures of dispersion are adopted to probe the upper tail of the distribution of  $Z$  (Figure 4). This includes the median  $\tilde{x}_Z$ , the median of the upper vigintiles  $\tilde{x}_{V_Z}$ , and  $Qn_Z$ , which is a robust measure of dispersion that is particularly robust for asymmetric distributions [Rousseeuw and Croux, 1993]. As represented in equation (7), those measures are used depending on the skewness  $\hat{S}$  of the distribution.

$$z_w = \begin{cases} \tilde{x}_{V_Z}, & \text{if } \hat{S} \leq 1 \\ \tilde{x}_Z + 3 * Qn_Z, & \text{if } \hat{S} > 1 \end{cases} \quad (7)$$

This approach was implemented and tested using 10 videos (i.e., 30 profiles) with different discharge and weather conditions. Figure 4 shows some representative examples for the distributions of  $Z$  that typically comprise a long tail toward higher elevation values. In some cases, it was observed that the upper tails of the distributions contain discontinuities which correspond to false positive detections in the water mask (Figure 4d). To address such cases, bins in the histogram which are disconnected from the main distribution

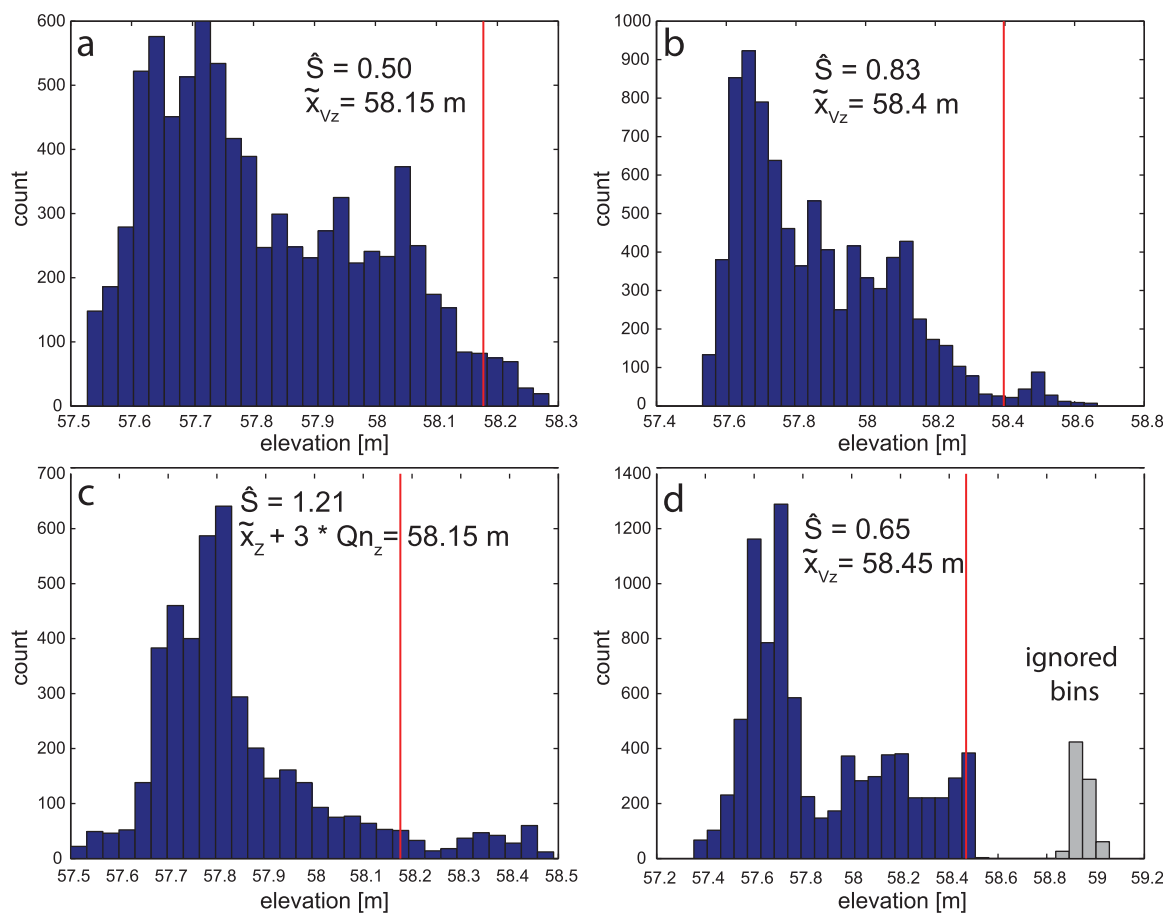


**Figure 4.** Four exemplary distributions of the bed elevation  $Z$  from the profiles presented in Figure 3. (a, b) Present cases with a skewness  $< 1$  where  $z_w = \tilde{x}_{Vz}$  and (c) a case where the skewness  $> 1$  and  $z_w = \tilde{x}_z + 3Q_{n_z}$ . (d) The histogram comprises empty bins with a total width  $> 10$  cm in which case bins on the right side of the gap are ignored.

by more than 10 cm are ignored. Figure 4 illustrates that the adopted statistics are effective to determine a water level value that is less affected by outliers.

### 3.6. Discharge Calculation and Depth-Average Coefficient

The measured surface velocity and the estimated water level can be combined with information on the metric footprint of the pixel on the ground (i.e., a local plane at  $z_w$ ) to calculate the discharge  $Q$  as the sum of the volume flow rates of all pixels along a particular profile. The measured surface velocities, however, have to be converted to depth-averaged velocities in order to account for the typically logarithmic vertical velocity profile. This can be achieved using a depth-average coefficient  $\alpha$  which is often assumed to be 0.85 but may vary between 0.72 and 0.93 depending on the site or experimental setup [Dramais et al., 2011; Muste et al., 2008; Le Coz et al., 2010; Polatel, 2006; Jodeau et al., 2008].

A total of nine independent discharge measurements were recorded at the site through classical current meter profiling of the stream. For security reasons, personal is not allowed to carry out measurements during torrential floods that usually coincide with the passing of tropical cyclones. The available measurements, therefore, represent discharge conditions of  $0.2 < Q < 2 \text{ m}^3 \text{ s}^{-1}$ . Normalizing the measured water elevations and velocities by the local water depths and depth-averaged velocities, respectively, a nondimensional vertical velocity profile is obtained. Following Le Coz et al. [2010], the profile is fitted with a logarithmic function to estimate a constant dimensionless velocity value near the free surface which is directly related to  $\alpha$ .

The result of this analysis (Figure 5a) shows a relatively steep velocity profile and suggests a value of  $\alpha = 0.88$ . Additionally, the relation between the discharge conditions and  $\alpha$  is investigated using the maximum water depth along the respective profile as a proxy for the flow regime. Considering the relatively few

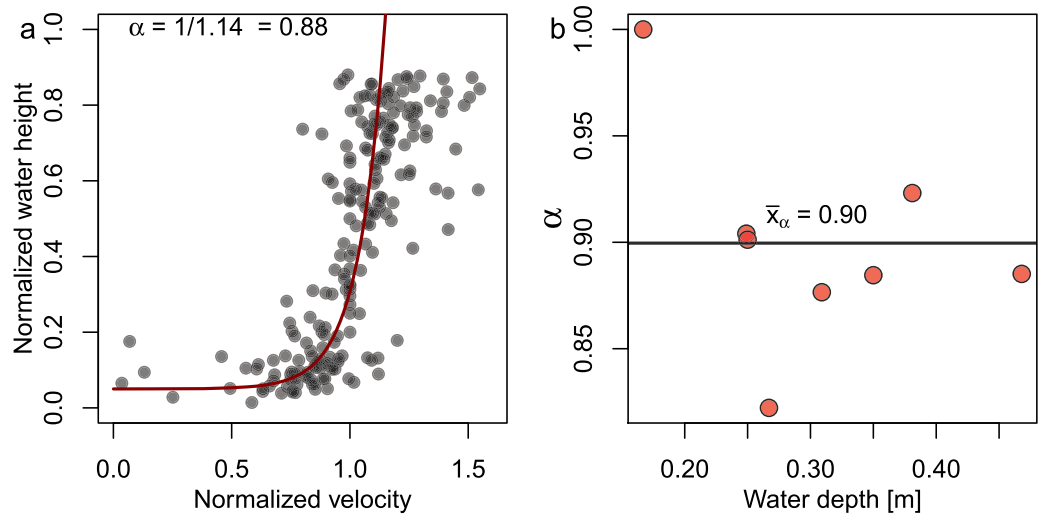


**Figure 5.** Empirical estimates of the depth-average coefficient  $\alpha$  using (a) a logarithmic approximation of the nondimensional vertical velocity profile and (b) the relationship of  $\alpha$  with the maximum water depth during the current meter measurement and the mean value of  $\alpha$  over all available measurements.

available measurements at low flow conditions, the analysis does not reveal a conclusive relationship between the flow regime (i.e., the water depth) and  $\alpha$  (Figure 5b) and suggests an average  $\alpha = 0.90$ , which is surprisingly high compared to previous LSPIV studies. The high  $\alpha$  could be related to the high roughness height at the site which might impede the formation of a logarithmic velocity profile at shallow flow depths [e.g., Manes et al., 2007]. An average value of  $\alpha = 0.89$  is adopted as a working hypothesis for the discharge calculation. To compute the discharge at a profile  $P$ , the image velocities are first projected perpendicular to the profile as expressed in equation (8) where  $\hat{p}$  denotes a unit vector perpendicular to the profile and  $\bar{v}'_{l_{xy}}$  is the scalar magnitude of the velocity after the projection in pixel  $s^{-1}$ .

$$\bar{v}'_{l_{xy}} = \frac{1}{n_m} \sum_{i=1}^{n_m} \frac{\Delta_{xy_i} \cdot \hat{p}}{\Delta t_i} \tag{8}$$

The discharge  $Q_p$  at the profile  $P$  can consequently be calculated using equation (9):

$$Q_p = \sum_{xy \in P} \bar{v}'_{l_{xy}} * \alpha * z_{xy} * A_{xy} \tag{9}$$

where  $\alpha$  is the dimensionless depth-average coefficient,  $z_{xy}$  is the water depth (in m) at the pixel  $xy$ , derived from the difference of the water level  $z_w$  and the riverbed DTM, and  $A_{xy}$  is the surface area of the pixel when projected to  $z_w$  in  $m^2 \text{ pixel}^{-1}$ .

While the  $\alpha$ -correction has the advantage that it yields a model for the physical structure of the flow, it cannot take into account a possible bias of the photogrammetric discharge measurements (e.g., systematic overestimation or underestimation of flow velocities or water height). To consider both the decreasing flow velocity with depth and a possible bias of the measurements, we propose an alternative technique to calibrate the system against the current measurements using a simple least square regression of the form:

$$\hat{Q}_p = \beta * Q_p + \gamma \tag{10}$$

Here  $\hat{Q}_p$  is the calibrated discharge and  $\beta$  and  $\gamma$  are the slope and the intercept of the regression, respectively. Taking into account  $Q_p$  (computed with  $\alpha = 1$ ) and the respective reference discharge  $Q_R$  obtained from current meter measurements, the slope and intercept are estimated in the least square sense as formulated in (11).

$$\min_{\beta, \gamma} \left( \sum_{i=1}^n (Q_{Ri} - \gamma - \beta * \hat{Q}_{Pi})^2 \right) \tag{11}$$

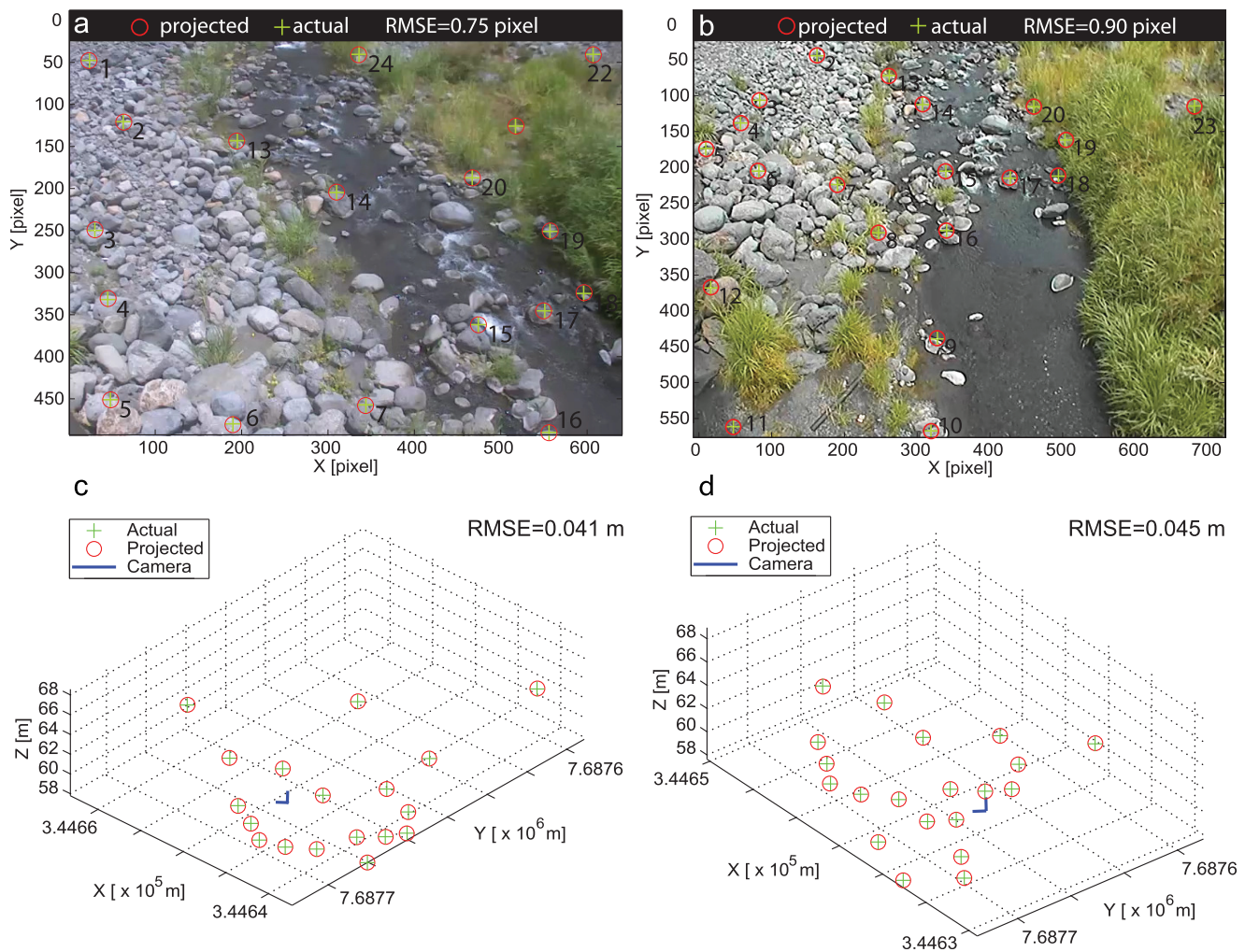


**Figure 6.** Residual reprojection errors of the ground control points in (a, b) image geometry and (c, d) ground geometry indicating an accuracy which is in the range of the dGNSS measurement uncertainty.

To assess the accuracy of the measurements after this calibration, we use a leave-one-out cross-validation to obtain an unbiased error estimate. The two calibration methods, being the use of a depth-average coefficient and the proposed statistical technique, are further referred to as  $\alpha$ -calibration and  $\beta$ -calibration, respectively.

As explained in section 3.5, each profile center line is intersected with a buffer of  $d_{xy} = 20$  pixels resulting in a total number of 40 subprofiles  $P_i$  per defined center line. *Dramais et al.* [2011] showed that measurements on different transects might deviate more than 4% and that water level errors of 10–50 cm can become the dominant error source  $Q$  by more than 20%. While some previous studies have already used spatial averaging techniques to reduce local errors in the flow field, measurements of  $Q$  are typically performed at only one single transect [*Muste et al.*, 2011, 2008; *Jodeau et al.*, 2008; *Le Coz et al.*, 2010; *Hauet et al.*, 2008b; *Kim et al.*, 2008]. Here we propose to analyze multiple profiles in an attempt to reduce the impact of local errors in the flow fields and water masks on the computed discharges. The many available profiles  $\{P_1, P_2 \dots P_n\}$  are used to compute average values and quantify the variance among the measurements  $\{Q_{P_1}, Q_{P_2} \dots Q_{P_n}\}$ . The median discharge  $\tilde{Q}_{P_n}$  and the interquartile range  $IQR_{P_n}$  are adopted as statistical estimates of the discharge and the measurement dispersion. Here  $n$  denotes the number of used profiles with  $n = 120$  if the cameras are analyzed separately and  $n = 240$  if measurements from both cameras are summarized. The ratio between the semi-interquartile range and the median discharge is adopted to quantify the dispersion of the discharge values among multiple profiles  $V_Q$ .

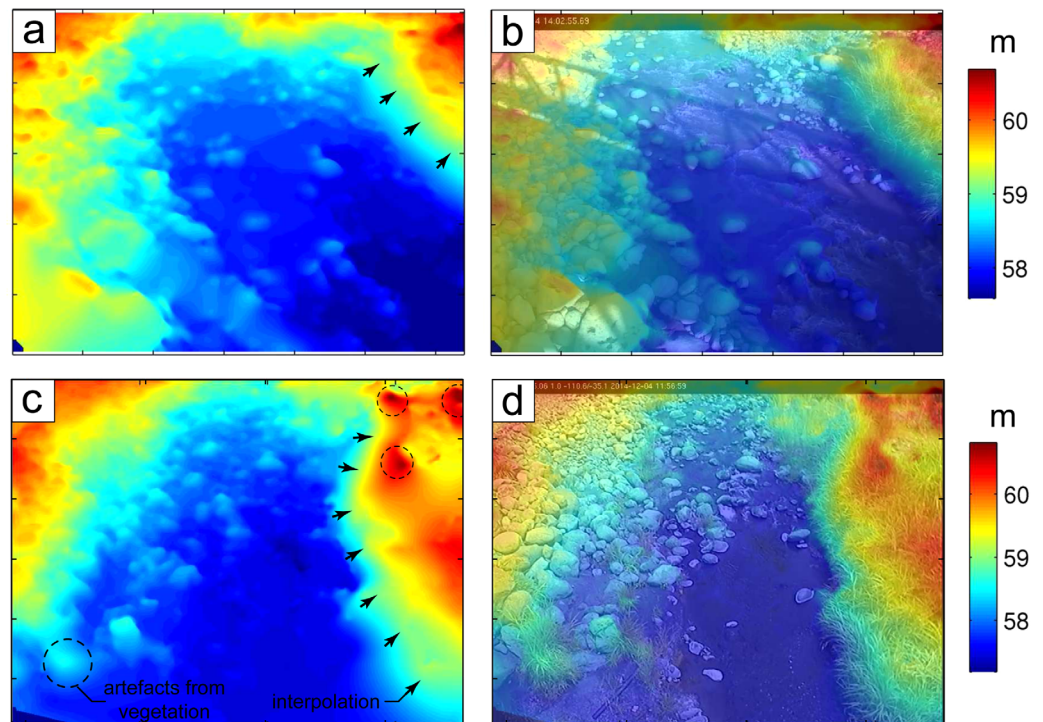


**Figure 7.** Projections of the DTMs in image geometry and overlay with simultaneously acquired video frames. (a) The projection of the DTM of 13 May 2014 (LiDAR) into the image geometry of Cam1 and (c) the projection of the DTM of 2 December 2014 (MVS) into the image geometry of Cam2. The projected DTMs are overlaid in (b, d) to illustrate the precise coregistration of the video frames and the surface models. Some artefacts resulting from vegetation and interpolation are notable.

$$V_Q = \frac{IQR_{P_n} \times 0.5}{Q_{P_n}} \times 100\% \quad (12)$$

## 4. Results and Discussion

### 4.1. Camera Calibration and Riverbed Topography

The accuracy of the obtained camera model is assessed by evaluating the reprojection residuals from ground coordinates to image coordinates and vice versa. Figures 6a and 6b show that the deviation between the image points and the projection of their 3-D coordinates into the image plane is generally less than 1 pixel and an RMSE between 0.75 and 0.90 pixel. Similarly, the inverse transformation results in an RMSE between 4.1 and 4.5 cm. Those figures are in the range of the uncertainties of the dGNSS measurements of 3.9 cm.

The quality of the coregistration of the DTMs with the cameras can be assessed visually through an overlay of the image on the projected DTMs as presented in Figures 7b and 7d. Small boulders depicted in the DTM match closely with the respective position in the camera images which indicates a successful coregistration. Since the camera calibration was carried out with GCPs recorded on 2 December 2014, whereas the LiDAR scans were georeferenced with GCPs collected 1 year later, changes in the camera parameters would be visible in the overlay presented in Figure 7b. The fact that no offset between the image and the DTM projection is apparent validates the stability of the camera parameters for this period. This is an important result since a need for frequent recalibration would hinder the long-term operational use of the proposed system.

Regarding the overall quality of the DTMs, it can be noted that the instrumental error of the employed LiDAR is less than 1 cm. For the MVS reconstruction, errors less than 5–10 cm can be expected at an imaging distance below 100 m [Stumpf *et al.*, 2015]. This margin could be confirmed through comparison of the MVS reconstruction against the LiDAR scans over stable terrain showing point distance with a standard deviation of 6 cm. In vegetated areas, some artifacts resulting from interpolation or incomplete vegetation filtering are apparent in Figures 7a and 7c.

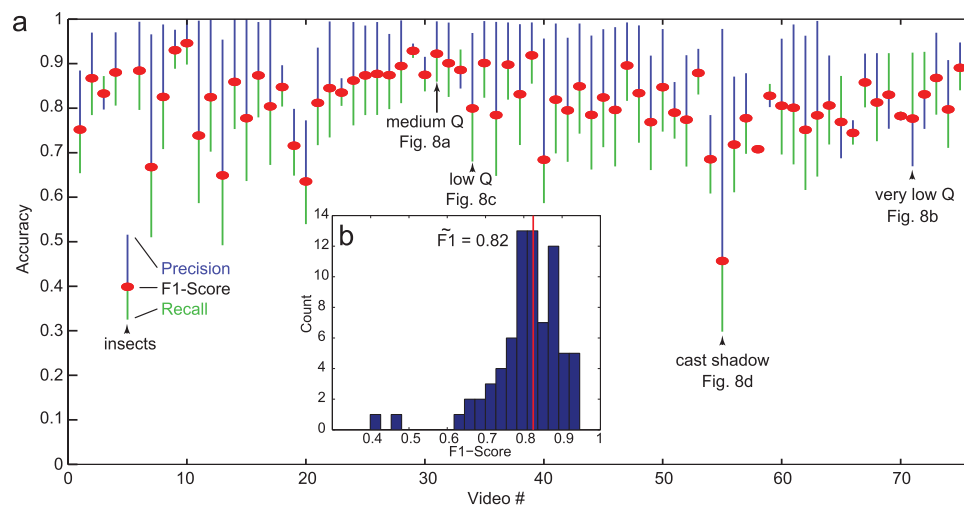


**Figure 8.** Accuracy of the water surface detection technique when tested against manually produced ground truth. (a) Precision, recall and F1-score for 75 tested videos. (b) Histogram and median of the F1-scores.

#### 4.2. Water Masks

The accuracy assessment of the water mask extraction on 74 videos shows that the technique yields a generally high precision and an acceptable recall (Figure 8a). For most of the tested videos, the F1-score is higher than 0.7 with a median of  $F1=0.82$  (Figure 8b). Considering the complex structure and variable environmental conditions of the study site, the proposed technique can be considered as relatively robust. However, two fail cases with  $F1 < 0.5$  can be clearly noted in Figure 8a. They are related to the presence of insects on the camera lens and the cast shadow of the bridge falling into the imaged area.

Based on an analysis of the dispersion of the discharge values among multiple profiles  $V_Q$  (section 4.4), we established  $V_{QMax} \leq 90.0\%$  as a threshold above which the dispersion is considered too high and the respective measurement is flagged as invalid. This allows to automatically eliminate several fail cases in the water mask detection, such as illustrated in Figures 9b and 9d. The water mask detection generally becomes less reliable at very low discharges ( $< 0.1 \text{ m}^3 \text{ s}^{-1}$ ) since the contrast between the measured flow velocity and noise on stable terrain diminishes, which leads to a breakdown of the thresholding technique and an overestimation of the water area (Figure 9b). At low discharges, problems can also arise from cast shadows which are prominent at the site before 6:30 in the morning and after 18:30 in the evening. They lead to saturation in sunlit parts of the image and low contrast in shaded areas (Figure 9d). Generally favorable results, however, are obtained for discharge conditions above  $0.5 \text{ m}^3/\text{s}$  (Figures 9a and 9c). Given that in most cases the precision of the water mask is higher than the recall, it must be expected that the technique underestimates the water surface area, the water level, and consequently the discharge.

#### 4.3. Calibration and Accuracy Assessment and Against Current Meter Measurements

To assess the accuracy of the system, the photogrammetric measurements are compared against classical current meter measurements for discharges between  $0.3$  and  $2 \text{ m}^3 \text{ s}^{-1}$ . The comparison presented in Figure 10 shows that, despite a high variance of the photogrammetric measurements, the median and the current meter measurements follow the same general trend. Using the classical  $\alpha$ -calibration to take into account the depth-velocity profile, however, leads to a systematic underestimation of the actual discharge and a mean absolute percentage error (MAPE) of 39.82% (Figure 10a). This is a direct result of the relatively lower recall of the water surface detection (Figure 8a) which accounts for an systematic underestimation of the discharge of 36.1% (supporting information, Figure S2).

Since this effect introduces a systematic error it can, however, be corrected using the regression-based  $\beta$ -calibration which reduces the MAPE to 9.00% and the maximum error to 19.74%. In this context, it is important to note again that this is an unbiased error estimate obtained by leave-one-out cross-validation. Considering its substantially better performance, the  $\beta$ -calibration was adopted to adjust all photogrammetric measurements. The fact that the MAPE of 9.00% is considerably below the variability of the discharges

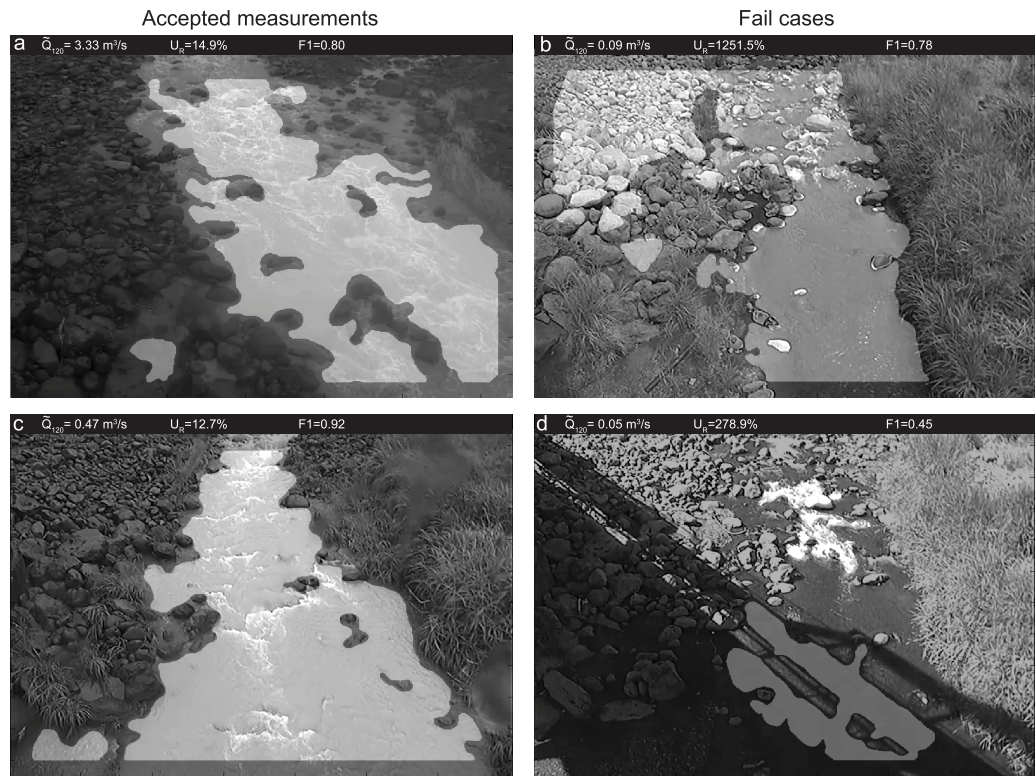


Figure 9. Exemplary results of the water detection technique at (a, c) low to medium flow and (b, d) fail cases due to very low flow and difficult illumination conditions.

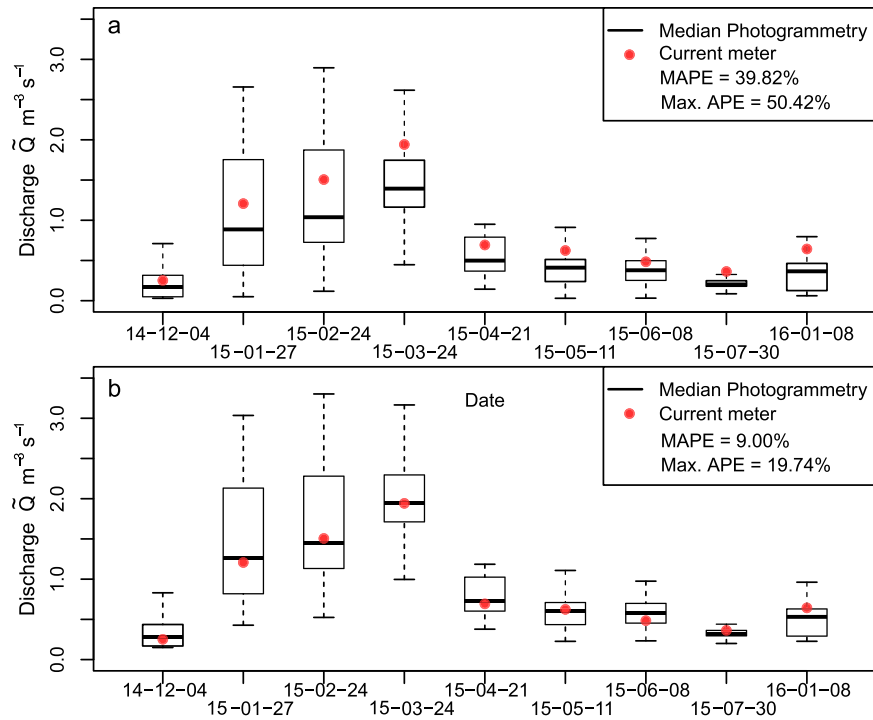


Figure 10. Comparison between the photogrammetric measurements and current meter profiling for nine different dates using (a)  $\alpha$ -calibration and (b)  $\beta$ -calibration with a leave-one-out cross-validation. The mean absolute percentage errors (MAPE) and maximum absolute percentage error (Max. APE) for both methods are indicated.

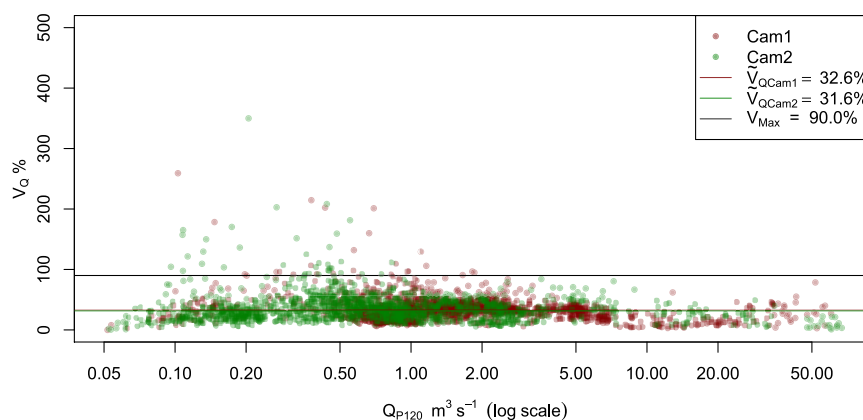


Figure 11. Measurement variance versus measured discharge for the two cameras.

among multiple profiles (see section 4.4) indicates that the spatiotemporal averaging of multiple profiles is indeed effective to account for a large part of random errors that might result from local errors in the DTMs, water masks or flow velocities. Overall the residual errors are very similar to results from previous LSPIV studies at various sites [Muste et al., 2014].

#### 4.4. Discharge Time Series

During the main monitoring period (15 December 2014 to 4 July 2015), a total of 3878 individual videos were recorded and analyzed. A total of 51 measurements were discarded since they were recorded at very low flow conditions yielding measurements below  $0.05 \text{ m}^3 \text{ s}^{-1}$ . At such low discharges, the flow becomes increasingly subcritical and free of traceable surface features which presents an inherent limitation for image-based velocimetry. A further number of 380 videos were discarded since they were recorded before 6:30 in the morning or after 18:30 when cast shadows and the general illumination did not allow reliable measurements. The remaining 3447 videos are used for a global analysis of the variability of the discharge values among multiple profiles (equation (12)).

Figure 11 shows the relationship between the discharge volume and the dispersion of the measured values. It illustrates that the dispersion is generally lower for larger discharges ( $>5 \text{ m}^3 \text{ s}^{-1}$ ) and increases toward lower volumes with an increased number of outliers, especially at discharges  $<2 \text{ m}^3 \text{ s}^{-1}$ . To avoid the inclusion of measurements with an excessively high dispersion, while still retaining most of the records, we used a threshold of  $V_{Q_{Max}} \leq 90.0\%$  which eliminates another 194 records. If all profiles are taken into account measurements from Cam2 feature a greater average dispersion of  $V_{Q_{Cam2}}=39.3\%$  which can be attributed to the fact that the near field view of Cam2 comprises a pond-like section of the stream where the turbulence of the flow reduces substantially (see Figure 3b). Under low discharge conditions, this leads to a lack of surface texture and an underestimation of the surface velocities and discharges. Removing the corresponding profile from the analysis yields  $V_{Q_{Cam2}}=31.6\%$  which is nearly identical to  $V_{Q_{Cam1}}=32.6\%$  (Figure 11). Consequently, the respective profile was removed from all further analyses.

During the test phase (2013–2014), the time series is still rather sparse and only three torrential flood events are captured (Figures 12a and 12b). The highest recorded discharge during this period amounts to  $70.1 \text{ m}^3 \text{ s}^{-1}$ . The hydrograph for the time period since January 2015 is constructed by aggregating measurements from both cameras at half-hourly intervals (Figures 12c). The measurements show the torrential flow regime of the river system with several flood events in particular from January to late March. The median of all measured discharges is  $0.86 \text{ m}^3 \text{ s}^{-1}$  which is considerably below the mean discharge of  $3.14 \text{ m}^3 \text{ s}^{-1}$ . The highest measured discharge in 2015 amounts to  $92.0 \text{ m}^3 \text{ s}^{-1}$  during the passage of the cyclone Haliba.

The flood events show a characteristic steeply rising limb of the hydrograph rising from less than  $1 \text{ m}^3 \text{ s}^{-1}$  to peak flow in less than 4 h. The peaks that can be observed in Figure 12c are directly related to several tropical cyclones of moderate to very high intensity including Bansi (8 January to 19 January), Chedza (13 January to 22 January) and Haliba (5 March to 12 March) of which especially the latter caused severe

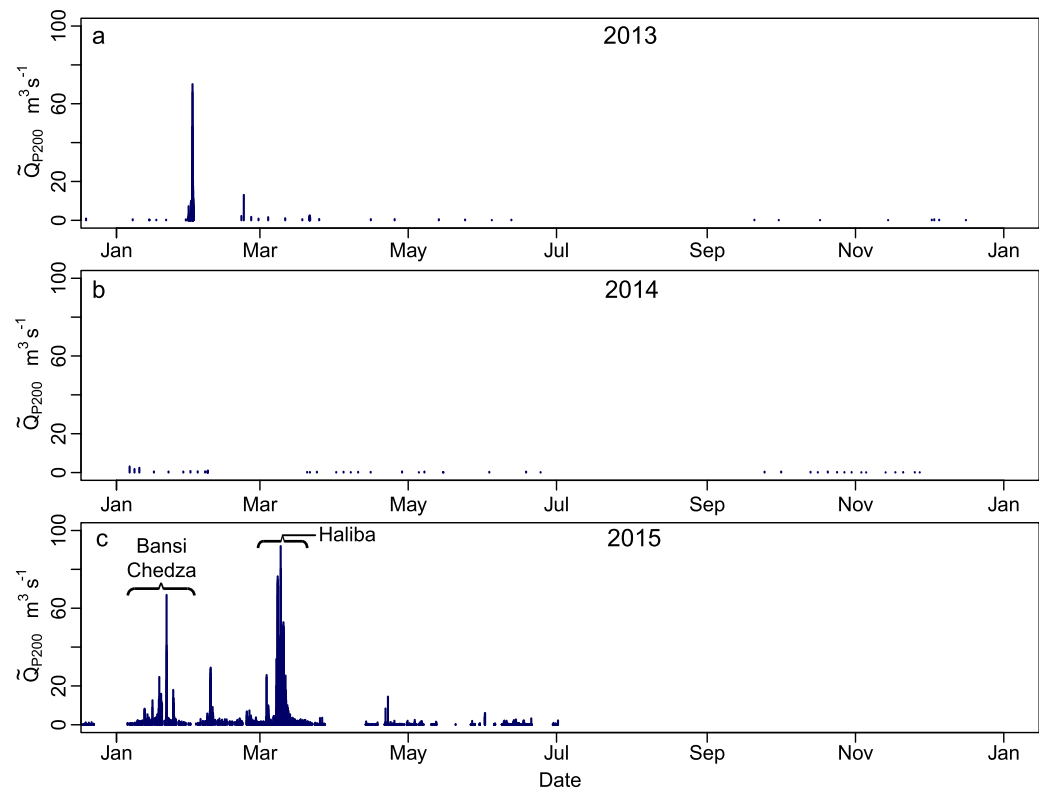


**Figure 12.** Discharge time series for the test phases in (a) 2013 and (b) 2014, and (c) the operational phase in 2015.

damage all over the island. Gaps in the time series in January and April 2015 are due to maintenance works on the system, while gaps between May and July 2015 are due to high  $V_0$  during periods of low discharge.

The highest discharge recorded during the measurement period ( $92.0 \text{ m}^3 \text{ s}^{-1}$ ) remains substantially below the 10 year flood peak discharge obtained from the analyses of pluviometric data, but is comparable to peak-discharge estimates ( $70 \text{ m}^3 \text{ s}^{-1}$ ) for the cyclone Hollanda in 1994 [Pouget and Garcin, 2003]. Given that the water surface area starts to approach the limit of the imaged areas at discharges  $>90 \text{ m}^3 \text{ s}^{-1}$ , the viewing geometry of the two analyzed cameras should probably be reconsidered to provide a better coverage during large flooding events exceeding  $100 \text{ m}^3 \text{ s}^{-1}$ .

Since the studied catchment is ungauged and field survey measurements during large rainstorms are not feasible, it remains challenging to quantify the accuracy of the obtained results for the torrential flood events. In order to provide at least a qualitative assessment of the discharges during large rainstorms, we consider pluviometric measurements from Plaine des Fougères station located at 1062 m within the same watershed approximately 7 km south of the bridge. The automated station records rainfall at 6 min intervals which are aggregated to 0.5 h intervals for a comparison with the photogrammetric discharge measurements. The correspondence between rain gauge records and  $Q$  for major floods in late January and early March is depicted Figure 13.

Figure 13a depicts the hydrograph resulting from a short and intense rainfall during the passage of cyclone Chedza, yielding a torrential flood with a steep rising limb and a peak discharge of  $67.4 \text{ m}^3 \text{ s}^{-1}$ . The lag time ( $T_L$ ) between the peak rainfall and peak discharge was approximately 1 h. Since there was almost no rainfall after the last video recording at the evening of 21 January, the falling limb of the hydrograph is interpolated to approximate the discharge during nighttime. Such an interpolation cannot be applied for the hydrograph recorded during the passage of the cyclone Haliba (Figure 13b) that yielded prolonged rainfalls with multiple peaks. The  $T_L$  between the first rainfall peak and peak discharge (7 March) was 1.5 h and increased for subsequent peaks to 2 h (8 March) and 4 h (9 March), respectively. In empirical formula, the  $T_L$  is often considered as a constant characteristic of the basin, although it is well known that it can vary

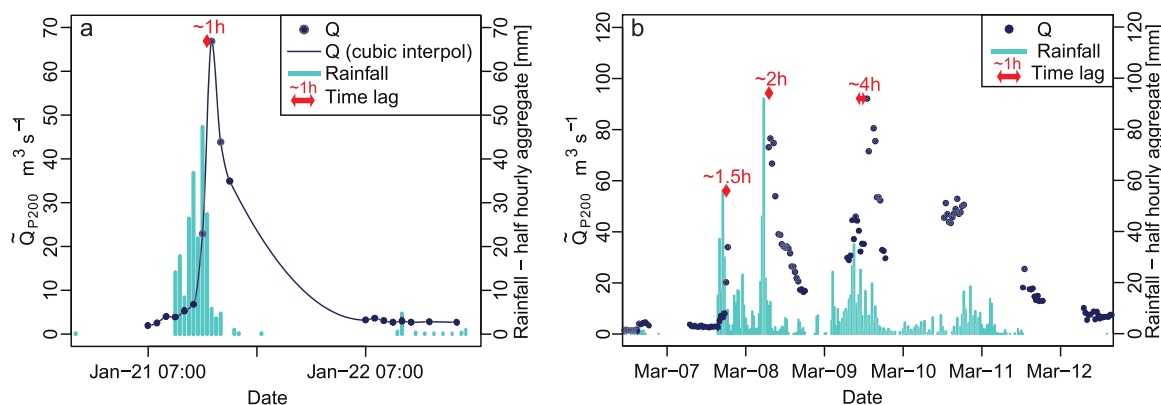


**Figure 13.** Comparison between discharge time series and rainfall measurements at the Plaine des Fougères pluviometric station for selected events. (a) Rainstorm during the passage of cyclone Chedza in late January 2015 and (b) sequence of rainstorms during the passage of cyclone Haliba in early March 2015.

considerably as a function of antecedent rainfalls and storm characteristics [Leopold, 1991; Muñoz-Villers and McDonnell, 2012; Haga *et al.*, 2005]. The limited number of analyzed events indicates an increase of the  $T_L$  with increasing rainfall duration and antecedent precipitation for the Rivières des Pluies. During the rising limb of the storm surges recorded in 2015, the discharge increased in average by  $13.7 \text{ m}^3 \text{ s}^{-1} \text{ h}^{-1}$ , whereas a maximum increase of  $56.8 \text{ m}^3 \text{ s}^{-1}$  within 1 h could be observed shortly before the peak discharge of  $92.0 \text{ m}^3 \text{ s}^{-1}$  at 13:30 on the 9 March.

Considering a simple relation between  $T_L$  and the time of concentration  $T_C$  where  $T_L = 0.6 \times T_C$  [Gercke and Smithers, 2014], and an upstream area of  $38.1 \text{ km}^2$ , a first-order estimate of the runoff coefficient can be proposed using the rational method. For the rainstorms presented in Figure 13, this yields runoff coefficients of 0.19, 0.14, 0.25, and 0.61, respectively. While these are only approximate figures that do not take into account the spatial variability within the catchment, nor a separation of the base flow, they are within the range of values reported for storm events in mountain catchments in the European Alps [e.g., Norbiato *et al.*, 2009].

The analysis of those flooding events suggests a good consistency between the rainfall and discharge measurements in terms of timing and magnitude but also exposes the lack of nighttime observations as an inherent limiting factor of photogrammetric river gauging. Especially for small torrential catchments such as Rivières des Pluies, this hinders the reconstruction of a continuous hydrograph and the inference of further catchment characteristics. Implications for a potential operational use of such a system and further developments are discussed in the next section.

#### 4.5. Potential and Limitations for Operational Use

Overall the analysis of the obtained results suggests a MAPE of 9% after the statistical calibration of the measurements. This figure is similar to results obtained in previous field studies in North America and Europe ranging from  $\pm 6\%$  [Bradley *et al.*, 2002] to  $\pm 10\%$  [Dramais *et al.*, 2011; Le Coz *et al.*, 2010; Hauet *et al.*, 2008b]. Considering that even under ideal conditions also reference measurements such as current meter profiling can bear important errors [Pelletier, 1988], those figures suggest that the proposed system and processing chain are sufficiently accurate for the monitoring of torrential tropical streams. The integrated algorithm for the water level detection from the video stream still requires further improvements to enhance its robustness and avoid the systematic underestimation of the stage ( $\sim 36\%$ ). However, in streams with violent floods where the use of pressure and radar gauges is often difficult, it can provide a viable alternative and circumvent the need for additional installations. The autonomous use of the system is only limited by the availability of suitable observation viewpoints (e.g., bridges) and the connections for power supply and data transmission. The developed processing chain requires less than 3 min per video on a standard desktop PC and allows to process multiple videos at the same time through parallel processing.

Despite the promising results, several further bottlenecks remain a need to be addressed before a broader operational use of the system. The most obvious limitation of any LSPIV system is the lack of nighttime measurements. The surveillance cameras used in this study have a nighttime modus but the resulting

videos do not sufficiently depict the texture of the water surface. Consequently, the use of artificial light sources such as LEDs appears indispensable to obtain continuous hydrographs through photogrammetric measurements. Surprisingly, yet very little research has been dedicated to this issue [Chaves, 2012].

Using LSPIV at rivers with high bed mobility imposes the need for frequent updates of the bed topography. The presented study shows that both terrestrial LiDAR and MVS are suitable techniques for repeated surveys. While MVS has many advantages in terms of costs and logistics, the processing of LiDAR data is still more straightforward. Both techniques, however, impose the need for visits at the site and additional processing by a skilled expert after major riverbed changes. The need for frequent topographic surveys could be circumvented by the use of multiple cameras with smaller baselines and the integration of robust stereo-matching algorithms to reconstruct the riverbed directly from videos acquired at low flow.

For the presented case study, the use of one single template size allowed to capture the flow features in both the foreground and background of the scene. In cases where the scene depth varies stronger, further modifications might be desirable to adapt the footprint of the template to the scale changes between foreground- and background.

The detection of the water surface is based on a number of assumptions on the image statistics which could be confirmed empirically for the study site but will probably require adaptations to achieve comparable performance at other sites. Improvements could certainly be achieved through dynamical adjustments of the parameters of the water mask detection according to the acquisition time or auxiliary data such as local weather forecasts. Also the acquisition frequency could be automatically increased to shorter time intervals (e.g., 5 min) when meteorological forecasts anticipate important rainfalls.

## 5. Conclusion

The presented study targeted the development and testing of a photogrammetric system for discharge monitoring with a particular focus on the automatic estimation of the water level and a long-term operational use at a challenging site along a torrential mountain river in the tropics. The proposed system presents several innovations including the consideration of radial lens distortion, a more efficient processing in image geometry, the automatic determination of the local water levels, and the estimation and calibration of the discharge based on multiple profiles and robust statistics. The study also presents on of the rare cases where LSPIV is used to measure torrential floods resulting from tropical cyclones.

An analysis of the obtained results suggests that the quality of the camera calibration reaches subpixel accuracy. The water mask detections has a median accuracy of  $F1=0.82$ , whereas the precision is systematically higher than the recall. The resulting underestimation of the water surface area and level leads to a systematic underestimation of the discharge and error rates of up to 50%. The bias can be effectively removed using a least square cross-calibration which reduces the error to an MAPE of 9% and a maximum error of 20%. Those error rates are considerably lower than the dispersion among multiple profiles (>30%) and illustrate the importance of the averaging among multiple measurements.

A total of 4218 videos spanning over 2.5 years were processed and allowed the reconstruction of long-term averages and several peak discharge events whose timing, magnitude, and runoff coefficients are consistent with simultaneous rainfall measurements. The presented case study demonstrates that photogrammetric measurements can provide accuracies and temporal frequencies which are already valuable for long-term, operational, day-time monitoring. This is especially true at sites with mobile riverbeds and violent torrential floods, which pose challenges for other established techniques such as ADCP and current meters. For a broader operational use of the photogrammetric discharge measurement system, we will focus on nighttime monitoring and a more adaptive and robust processing chain for the water surface detection.

## References

- Baldassarre, G. D., and A. Montanari (2009), Uncertainty in river discharge observations: A quantitative analysis, *Hydrol. Earth Syst. Sci.*, 13(6), 913–921.
- Bradley, A. A., A. Kruger, E. A. Meselhe, and M. V. Muste (2002), Flow measurement in streams using video imagery, *Water Resour. Res.*, 38(12), 1315, 51–1.
- Chan, T. F., and L. Vese (2001), Active contours without edges, *IEEE Trans. Image Process.*, 10(2), 266–277.

### Acknowledgments

We thankfully acknowledge the financial support of the Office de l'eau Réunion through the INTRACRUE project on operational systems for discharge and sediment transfer monitoring at La Réunion. We are also grateful to our colleagues Jerome Ammann, Réjanne Le Bivic, and Eric Delcher for the help in the field at several occasions and Pascal Allemand for initial ideas and code for the image processing chain. A demo of the described techniques which allows to reproduce some of the presented results and figures is available at <https://bitbucket.org/AndreStumpf/photogrammetricdischargedemo>. The complete video data set is available from the authors upon request (andre.stumpf@unistra.fr).

- Chaves, H. (2012), A weather independent illumination for field LSPIV, paper presented at 16th International Symposium on Applications of Laser Techniques to Fluid Mechanics, Lisbon, Portugal. [Available at [http://lctes.dem.ist.utl.pt/lxaser/lxaser2012/sponsors\\_partners.asp](http://lctes.dem.ist.utl.pt/lxaser/lxaser2012/sponsors_partners.asp)]
- Creutin, J., M. Muste, A. Bradley, S. Kim, and A. Kruger (2003), River gauging using PIV techniques: A proof of concept experiment on the Iowa River, *J. Hydrol.*, *277*(3), 182–194.
- Dramais, G., J. Le Coz, B. Camenen, and A. Hauet (2011), Advantages of a mobile LSPIV method for measuring flood discharges and improving stage–discharge curves, *J. Hydro-environ. Res.*, *5*(4), 301–312.
- ffmpeg.org (2015), *FFmpeg* 2.8. [Available at <https://www.ffmpeg.org>]
- Fujita, I., M. Muste, and A. Kruger (1998), Large-scale particle image velocimetry for flow analysis in hydraulic engineering applications, *J. Hydraul. Res.*, *36*(3), 397–414.
- Fujita, I., H. Watanabe, and R. Tsubaki (2007), Development of a non-intrusive and efficient flow monitoring technique: The space-time image velocimetry (STIV), *Int. J. River Basin Manage.*, *5*(2), 105–114.
- Garcin, M., B. Poisson, and R. Pouget (2005), High rates of geomorphological processes in a tropical area: The Remparts River case study (Réunion Island, Indian Ocean), *Geomorphology*, *67*(3), 335–350.
- Gericke, O. J., and J. C. Smithers (2014), Review of methods used to estimate catchment response time for the purpose of peak discharge estimation, *Hydrol. Sci. J.*, *59*(11), 1935–1971.
- Haga, H., Y. Matsumoto, J. Matsutani, M. Fujita, K. Nishida, and Y. Sakamoto (2005), Flow paths, rainfall properties, and antecedent soil moisture controlling lags to peak discharge in a granitic unchanneled catchment, *Water Resour. Res.*, *41*, W12410, doi:10.1029/2005WR004236.
- Hamilton, A., and R. Moore (2012), Quantifying uncertainty in streamflow records, *Can. Water Resour. J.*, *37*(1), 3–21.
- Hartley, R., and A. Zisserman (2004), *Multiple View Geometry in Computer Vision*, 2nd ed., Cambridge University Press, Cambridge, U. K.
- Hauet, A., J.-D. Creutin, and P. Belleudy (2008a), Sensitivity study of large-scale particle image velocimetry measurement of river discharge using numerical simulation, *J. Hydrol.*, *349*(1–2), 178–190, doi:10.1016/j.jhydrol.2007.10.062.
- Hauet, A., A. Kruger, W. Krajewski, A. Bradley, M. Muste, J. Creutin, and M. Wilson (2008b), Experimental system for real-time discharge estimation using an image-based method, *J. Hydrol. Eng.*, *13*(2), 105–110, doi:10.1061/(ASCE)1084-0699(2008)13:2(105).
- He, H., and E. Garcia (2009), Learning from imbalanced data, *IEEE Trans. Knowledge Data Eng.*, *21*(9), 1263–1284.
- Heritage, G., and D. Hetherington (2007), Towards a protocol for laser scanning in fluvial geomorphology, *Earth Surf. Processes Landforms*, *32*(1), 66–74.
- Inglada, J., V. Muron, D. Pichard, and T. Feuvrier (2007), Analysis of artifacts in subpixel remote sensing image registration, *IEEE Trans. Geosci. Remote Sens.*, *45*(1), 254–264.
- Jodeau, M., A. Hauet, A. Paquier, J. Le Coz, and G. Dramais (2008), Application and evaluation of LS-PIV technique for the monitoring of river surface velocities in high flow conditions, *Flow Meas. Instrum.*, *19*(2), 117–127, doi:10.1016/j.flowmeasinst.2007.11.004.
- Kim, Y. (2006), Uncertainty analysis for non-intrusive measurement of river discharge using image velocimetry, PhD thesis, Univ. of Iowa, Iowa.
- Kim, Y., M. Muste, A. Hauet, W. F. Krajewski, A. Kruger, and A. Bradley (2008), Stream discharge using mobile large-scale particle image velocimetry: A proof of concept, *Water Resour. Res.*, *44*, W09502, doi:10.1029/2006WR005441.
- Le Boursicaud, R., L. Pénard, A. Hauet, F. Thollet, and J. Le Coz (2016), Gauging extreme floods on YouTube: Application of LSPIV to home movies for the post-event determination of stream discharges, *Hydrol. Processes*, *30*(1), 90–105.
- Le Coz, J., A. Hauet, G. Pierrefeu, G. Dramais, and B. Camenen (2010), Performance of image-based velocimetry (LSPIV) applied to flash-flood discharge measurements in Mediterranean rivers, *J. Hydrol.*, *394*(1), 42–52.
- Legout, C., F. Darboux, Y. Nédélec, A. Hauet, M. Esteves, B. Renaux, H. Denis, and S. Cordier (2012), High spatial resolution mapping of surface velocities and depths for shallow overland flow, *Earth Surf. Processes Landforms*, *37*(9), 984–993.
- Leopold, L. B. (1991), Lag times for small drainage basins, *Catena*, *18*(2), 157–171.
- Manes, C., D. Pokrajac, and I. McEwan (2007), Double-averaged open-channel flows with small relative submergence, *J. Hydraul. Eng.*, *133*(8), 896–904.
- MathWorks (2014), *Matlab Version 8.3.0.532 (R2014a)*, Natick, Mass.
- McMillan, H., T. Krueger, and J. Freer (2012), Benchmarking observational uncertainties for hydrology: Rainfall, river discharge and water quality, *Hydrol. Processes*, *26*(26), 4078–4111.
- Milliman, J. D. (1995), Sediment discharge to the ocean from small mountainous rivers: the New Guinea example, *Geo Mar. Lett.*, *15*(3–4), 127–133.
- Milliman, J. D., and K. L. Farnsworth (2011), *River Discharge to the Coastal Ocean: A Global Synthesis*, Cambridge University Press, Cambridge, U. K.
- Muñoz-Villers, L. E., and J. J. McDonnell (2012), Runoff generation in a steep, tropical montane cloud forest catchment on permeable volcanic substrate, *Water Resour. Res.*, *48*, W09528, doi:10.1029/2011WR011316.
- Muste, M., I. Fujita, and A. Hauet (2008), Large-scale particle image velocimetry for measurements in riverine environments, *Water Resour. Res.*, *44*, W00D19, doi:10.1029/2008WR006950.
- Muste, M., H.-C. Ho, and D. Kim (2011), Considerations on direct stream flow measurements using video imagery: Outlook and research needs, *J. Hydro-environ. Res.*, *5*(4), 289–300.
- Muste, M., A. Hauet, I. Fujita, C. Legout, and H.-C. Ho (2014), Capabilities of large-scale particle image velocimetry to characterize shallow free-surface flows, *Adv. Water Resour.*, *70*(0), 160–171, doi:10.1016/j.advwatres.2014.04.004.
- Norbato, D., M. Borga, R. Merz, G. Blöschl, and A. Carton (2009), Controls on event runoff coefficients in the eastern Italian Alps, *J. Hydrol.*, *375*(3), 312–325.
- Novatel (2014), *GrafNav / GrafNet 8.60 - A Novatel Precise Positioning Product User Guide*, Rev 3, 192 pp., Novatel Inc., Calgary, Alberta. [Available at [http://www.novatel.com/assets/Documents/Waypoint/Downloads/NavNet860\\_Manual.pdf](http://www.novatel.com/assets/Documents/Waypoint/Downloads/NavNet860_Manual.pdf)]
- Otsu, N. (1975), A threshold selection method from gray-level histograms, *Automatica*, *11*(285–296), 23–27.
- Ouédraogo, M. M., A. Degré, C. Debouche, and J. Lisein (2014), The evaluation of unmanned aerial system-based photogrammetry and terrestrial laser scanning to generate DEMs of agricultural watersheds, *Geomorphology*, *214*(0), 339–355, doi:10.1016/j.geomorph.2014.02.016.
- Parsons, D., P. Jackson, J. Czuba, F. Engel, B. Rhoads, K. Oberg, J. Best, D. Mueller, K. Johnson, and J. Riley (2013), Velocity mapping toolbox (VMT): A processing and visualization suite for moving-vessel ADCP measurements, *Earth Surf. Processes Landforms*, *38*(11), 1244–1260.
- Pelletier, P. M. (1988), Uncertainties in the single determination of river discharge: A literature review, *Can. J. Civil Eng.*, *15*(5), 834–850.

- Pierrot-Deseilligny, M., and I. Clery (2011), APERO, an open source bundle adjustment software for automatic calibration and orientation of set of images, in *International Archives of the Photogrammetry, Remote Sensing and Spatial Information Science*, vol. XXXVIII-5/W16, pp. 1–8, ISPRS, Trento, Italy.
- Pierrot-Deseilligny, M., J. Belveaux, G. Choqueux, M. Deveau, and L. Girod (2015), *MicMac, Apero and Other Beverages in a Nutshell*, ENSG, Marne-la-Vallée, France.
- Polatel, C. (2006), Large-scale roughness effect on free-surface and bulk flow characteristics in open-channel flows, PhD thesis, Univ. of Iowa, Iowa.
- Pouget, R., and M. Garcin (2003), Etude diagnostic du transport solide et de l'évolution du fond du lit de la rivière des Pluies, Ile de La Réunion, *Proj. Serv. Public BRGM 03 RES 837 BRGMIRP-52841 -FR*, BRGM, BRGM, Orleans, La Réunion, France.
- Ran, Q.-h., W. Li, Q. Liao, H.-l. Tang, and M.-y. Wang (2016), Application of an automated LSPV system in a mountainous stream for continuous flood flow measurements, *Hydrol. Processes*, doi:10.1002/hyp.10836, in press.
- Remondino, F., and C. Fraser (2006), Digital camera calibration methods: Considerations and comparisons, *Int. Arch. Photogramm. Remote Sens.*, 36(5), 266–272.
- Rousseeuw, P. J., and C. Croux (1993), Alternatives to the median absolute deviation, *J. Am. Stat. Assoc.*, 88(424), 1273–1283.
- Salvi, J., X. Armangué, and J. Batlle (2002), A comparative review of camera calibrating methods with accuracy evaluation, *Pattern Recognition*, 35(7), 1617–1635, doi:10.1016/S0031-3203(01)00126-1.
- Sibson, R. (1981), A brief description of natural neighbour interpolation (Chapter 2), in *Interpreting Multivariate Data*, edited by V. Barnett, pp. 21–36, Wiley, Chichester.
- Stumpf, A., J.-P. Malet, N. Kerle, U. Niethammer, and S. Rothmund (2013), Image-based mapping of surface fissures for the investigation of landslide dynamics, *Geomorphology*, 186(0), 12–27, doi:10.1016/j.geomorph.2012.12.010.
- Stumpf, A., J.-P. Malet, P. Allemand, M. Pierrot-Deseilligny, and G. Skupinski (2015), Ground-based multi-view photogrammetry for the monitoring of landslide deformation and erosion, *Geomorphology*, 231(0), 130–145, doi:10.1016/j.geomorph.2014.10.039.
- Tsai, R. (1987), A versatile camera calibration technique for high-accuracy 3D machine vision metrology using off-the-shelf TV cameras and lenses, *IEEE J. Robotics Autom.*, 3(4), 323–344, doi:10.1109/JRA.1987.1087109.
- Tsubaki, R., I. Fujita, and S. Tsutsumi (2011), Measurement of the flood discharge of a small-sized river using an existing digital video recording system, *J. Hydro-environ. Res.*, 5(4), 313–321.
- Villeneuve, N., P. Bachèlery, and J. Kemp (2014), La Réunion island: A typical example of a basaltic shield volcano with rapid evolution, in *Landscapes and Landforms of France, World Geomorphol. Landscapes*, edited by M. Fort and M.-F. André, pp. 261–270, Springer, Netherlands, Dordrecht.
- Welber, M., J. Le Coz, J. B. Laronne, G. Zolezzi, D. Zamler, G. Dramais, A. Hauet, and M. Salvaro (2016), Field assessment of noncontact stream gauging using portable surface velocity radars (SVR), *Water Resour. Res.*, 1108–1126, doi:10.1002/2015WR017906.
- Willert, C. E., and M. Gharib (1991), Digital particle image velocimetry, *Exp. Fluids*, 10(4), 181–193.